

MXene-derived C-doped TiO₂/Ti₃C₂ heterojunction as a high-performance visible-light photocatalyst

Kai Chen

Wuhan University of Science and Technology

Kang Yan

Wuhan University of Science and Technology

Qun Xie

Wuhan University of Science and Technology

Hui Zhu

Wuhan University of Science and Technology

Xuanke Li

Wuhan University of Science and Technology

Zhijun Dong

Wuhan University of Science and Technology

Guanming Yuan

Wuhan University of Science and Technology

Jiang Zhang

Wuhan University of Science and Technology

Ye Cong (✉ congye@wust.edu.cn)


Wuhan University of Science and Technology

Research Article

Keywords: Ti₃C₂ MXene, TiO₂/Ti₃C₂, Photocatalysis, In-situ oxidation

Posted Date: July 11th, 2022

DOI: <https://doi.org/10.21203/rs.3.rs-1806462/v1>

License:  This work is licensed under a Creative Commons Attribution 4.0 International License. [Read Full License](#)

Abstract

Fabrication TiO_2 with conductive two-dimensional materials is an effective strategy to improve its photocatalytic activity. Herein, a well-defined carbon doped $\text{TiO}_2/\text{Ti}_3\text{C}_2$ heterojunction is constructed via in-situ controllable oxidation of Ti_3C_2 MXene in carbon dioxide. The formed carbon doped TiO_2 nanoparticles as the photocatalyst uniformly disperse on the surface of Ti_3C_2 MXene and generate electrons and holes under the irradiation. The two-dimensional Ti_3C_2 MXene, ascribing to its excellent conductivity, acts as the electron transport channels and accelerates the separation of photo-generated electrons and holes. Meanwhile, due to its large specific surface area and good solubility, Ti_3C_2 MXene may facilitate to enhance the adsorption of pollutant on the photocatalyst as well as the absorption of photocatalyst for visible light. Therefore, the unique properties of TiO_2 and Ti_3C_2 MXene are integrated in a complementary way and significantly improve the photocatalytic performance of the composites. The proper content of Ti_3C_2 MXene and TiO_2 in the composite is crucial for enhancing the photocatalytic performance, which can be effectively tuned by varying the oxidation temperature. In this work, C- $\text{TiO}_2/\text{Ti}_3\text{C}_2$ oxidized at 400 °C presents the optimum photocatalytic performance.

Introduction

MXene is a new type of two-dimensional (2D) transition metal carbide, nitride and carbonitride nanomaterials. It has aroused special attention in the fields of energy storage, adsorption and catalysis due to its fantastic structure and properties, including large specific surface area, rich layer structure, excellent conductivity, tunable optical and electronic property and reversible embedding performance of metal cations[1–4]. Ti_3C_2 MXene, as the most important member of MXene family is generally obtained by etching the Al atoms from Ti_3AlC_2 with hydrofluoric acid or a mixture of fluoride and hydrochloric acid, the surface of which is loaded with O, OH or F groups[5–7]. It is worthy to note that its intrinsic characteristics, such as zero band gap and lower photoelectric conversion rate, make bare metallic Ti_3C_2 hard to be an ideal photocatalyst[8]. However, Ti_3C_2 MXene can act as a good candidate for photocatalyst because of its high conductivity, large surface area, hydrophilicity and modifiable bandgap with variable terminating functional groups[9–12].

Photocatalysis technique has always been considered as one of the most promising approaches to relieve the environmental pollution and energy problems[13–15]. The combination of TiO_2 with 2D materials such as graphene can greatly improve the performance of TiO_2 photocatalyst. Zhang et al. [16] synthesized a series of TiO_2 /graphene composites with different graphene contents by sol method, which greatly ameliorated the photocatalytic activity of TiO_2 . Considering the similar two-dimensional structure of Ti_3C_2 MXene with graphene, the integration of Ti_3C_2 MXene and TiO_2 is promising to construct high-performance photocatalyst. Naguib and his co-workers reported TiO_2 -disordered graphitic carbon hybrid structures by flashing oxidation of 2D Ti_3C_2 in air[17]. The oxidation processes in CO_2 and pressurized water were also discussed. But the transient flashing oxidation process is difficult to control, and the sample powder may be ignited during the transient oxidation process. The $\text{TiO}_2/\text{Ti}_3\text{C}_2$ composites were also prepared by hydrothermal oxidation of Ti_3C_2 MXene, which showed higher catalytic activity than pure Ti_3C_2 and TiO_2 [18, 19]. Ahmed et al. oxidized Ti_2C MXene with hydrogen peroxide solution to grow TiO_2 nanocrystals on the surface of Ti_2C sheets[20]. The oxidation was exceedingly rapid and the small product was hard to be collected due to the strong oxidizing ability of hydrogen peroxide solution. Yuan et al. modulated Ti_3C_2 MXene at high temperatures (above 700 °C) to form C/ TiO_2 Hybrids[21]. The result showed that band gap of C/ TiO_2 hybrids was slightly narrower than that of pure TiO_2 . Unfortunately, oxidation at higher

temperature will destroy the layered structure of Ti_3C_2 MXene and result in most of Ti_3C_2 transferring to amorphous carbon, which undoubtedly will weaken the positive effects of Ti_3C_2 and reduce the conductivity of the material. Moreover, carbon monoxide gas is generated by oxidation at high temperature, which makes the experiment dangerous. Consequently, controlling the oxidation of Ti_3C_2 MXene at low temperature in CO_2 atmosphere is an appealing approach to get $\text{TiO}_2/\text{Ti}_3\text{C}_2$ composite materials with variable components, meeting their requirements as photocatalysts by combination the merits of TiO_2 and Ti_3C_2 .

In this paper, we focus on the controlling oxidation of Ti_3C_2 in CO_2 at relative lower temperature to prepare $\text{TiO}_2/\text{Ti}_3\text{C}_2$ composites. The components and surface microstructure of TiO_2 and Ti_3C_2 in the composites can be tuned by varying the oxidation temperature. Correspondingly, Ti_3C_2 MXene can effectively retain and contribute its auspicious effects in photocatalytic reactions. TiO_2 crystals formed by oxidation Ti_3C_2 MXene can produce photogenerated hole-electron pairs, and the unique two-dimensional layered structure can provide electron transport channels and improve the separating efficiency of electrons and holes. Moreover, carbon doping generated by the transformation of Ti_3C_2 MXene may play positive roles for enhancing the activity of TiO_2 . The effects of different oxidation temperatures on structure of $\text{TiO}_2/\text{Ti}_3\text{C}_2$ composites and photocatalytic degradation for Rhodamine B solution were systematically investigated. It may lay a foundation for the research of Ti_3C_2 MXene in the field of photocatalysis and provide a reference for studying other similar materials.

Experimental

Preparation of Ti_3C_2 MXene

Ti_3C_2 MXene multilayer materials was prepared by chemical etching of Ti_3AlC_2 powder (400 mesh) in hydrofluoric acid solution following a typical procedure as previously described[22]. A total of 1 g Ti_3AlC_2 powder was gradually added into 20 mL of hydrofluoric acid (HF, 49%), magnetically stirring for 24 h at 30°C. The mixture was then centrifuged, and the sediment was washed several times with deionized water until the pH reached about 6. Then the final product was dried in a vacuum oven at 60 ° C for 24 h to get Ti_3C_2 MXene powder.

Preparation of $\text{TiO}_2/\text{Ti}_3\text{C}_2$ composites

0.2 g of as-prepared Ti_3C_2 MXene powder was put into corundum crucible and placed in a horizontal tube furnace. After purging by argon gas for 20 minutes, the temperature of the tube furnace was raising to the target temperature at a heating rate of 10 °C min⁻¹. Subsequently, CO_2 (gas flow rate of 50 sccm) was used as an oxidant to replace argon gas and the target temperature was kept constant for 1 h, where the target temperatures were 300 °C, 400 °C, 500 °C, 600 °C, and 700 °C, respectively. After oxidation process, argon gas was maintained to cool down the furnace to room temperature. The as-prepared products were labeled as $\text{TiO}_2/\text{Ti}_3\text{C}_2$ -*T*, where *T* presented the oxidation temperature. The preparation process of $\text{TiO}_2/\text{Ti}_3\text{C}_2$ composites is illustrated in Fig. 1.

Characterization of materials

The phase composition of the material was analyzed by X-ray diffraction (XRD) measurement using a Bruker A X'Pert PRO MPD type target X-ray powder diffractometer. Scanning electron microscopy (SEM) was used to investigate the morphology on Nova 400 NanoSEM with the operating voltage of 30 kV. The microstructure of the materials was characterized by field emission transmission electron microscope (FE-TEM, FEI Tecnai G2 F20 S-

TWIN) with an accelerating voltage of 120 kV. Raman spectroscopy was recorded by Raman spectrometer (LabRam HR Evolution) to testify the molecular structure of materials. X-ray photoelectron spectroscopy (XPS) was performed to study the elemental composition and chemical states on ThermoFischer ESCALAB 250XI. ASAP 2020 physical adsorber was carried out to measure the specific surface area. UV-visible diffuse reflectance spectroscopy was performed on the Shimadzu UV-2550PC UV-Vis spectrophotometer to determine the light absorption properties of the photocatalyst. The separating efficiency of electrons and holes of the photocatalyst was analyzed by fluorescence spectroscopy with Hitachi F-7000 fluorescence spectrophotometer.

Photocatalytic activity measurement

In a typical process, 0.1 g photocatalyst was added into 100 mL of Rhodamine B solution (30 mg L^{-1}). Before irradiated under visible light, the solution was stirring in a dark environment for 3 h until the adsorption/desorption equilibrium. A 300 W Xenon lamp with a cut-off filter ($\lambda \geq 420 \text{ nm}$) was used as the irradiation source. During the photodegradation, 4 mL suspension was collected at a certain interval and centrifuged to remove the residual photocatalyst. Then the solution was analyzed on X3PC UV-Vis spectrophotometer to determine the degradation rate for Rhodamine B.

Results And Discussion

Phase and morphology analysis of Ti_3C_2 MXene

The XRD patterns of Ti_3AlC_2 and Ti_3C_2 MXene are illustrated in Fig. 2. The sharp diffraction peak at $2\theta \approx 9.5^\circ$ belongs to the characteristic diffraction peak of Ti_3AlC_2 , corresponding to the (002) crystal plane of Ti_3AlC_2 . The other diffraction peaks at $2\theta \approx 34.0^\circ$, 39.0° , 41.8° and 60.2° are ascribed to the (101), (104), (105) and (110) plane of Ti_3AlC_2 (JCPDS:00-052-0875), respectively. A weak diffraction peak at $2\theta \approx 35.9^\circ$ corresponds to the (111) crystal plane of TiC (JCPDS: 00-031-1400), which is due to trace amounts of TiC residual during the synthesis of Ti_3AlC_2 . After hydrofluoric acid etching, the diffraction peaks of Ti_3AlC_2 disappear, and new diffraction peaks appear at $2\theta \approx 8.5^\circ$, 18.2° , 27.5° , 33.1° , 42.1° and 61.4° , corresponding to the (002), (006), (008), (0010), (0012) and (110) crystal planes of Ti_3C_2 MXene, respectively. It confirms that Ti_3AlC_2 has transformed to Ti_3C_2 MXene after etching in hydrofluoric acid solution. This is due to that the Ti-C bonds in Ti_3AlC_2 are mainly covalent bonds and ionic bonds; while the Ti-Al and Al-Al bonds are mainly metal bonds, and the strength of which is weaker than that of Ti-C bond. So Ti_3AlC_2 would be more likely to strip off the Al atoms after being treated with hydrofluoric acid. Moreover, the diffraction peak of Ti_3AlC_2 at $2\theta \approx 9.5^\circ$ shifts to lower angle after the etching, indicating the increasing of the interlayer spacing of the material.

Figure 3 is SEM images of Ti_3AlC_2 and Ti_3C_2 MXene. As can be seen from Fig. 3, the as-synthesized Ti_3AlC_2 shows a typical ternary layered structure of the MAX phase. After treatment with hydrofluoric acid, the morphology of Ti_3AlC_2 changes significantly. The ternary layered structure of Ti_3AlC_2 is peeled off and manifests the typical accordion-like morphology with stacked layers and smooth surface.

Composition and structure analysis of $\text{TiO}_2/\text{Ti}_3\text{C}_2$ MXene

The XRD patterns of $\text{TiO}_2/\text{Ti}_3\text{C}_2$ MXene after oxidation in CO_2 at different temperatures are presented in Fig. 4. It is obvious that when the oxidation temperature is lower than 700°C , the diffraction peaks are mainly attributed to Ti_3C_2 MXene, accompanied by the weak diffraction peak ($2\theta \approx 25.5^\circ$) of the crystal plane of TiO_2 . This implies the

co-existence of Ti_3C_2 MXene and ultrafine TiO_2 . With the increase of oxidation temperature, the intensities of the diffraction peaks of Ti_3C_2 MXene gradually decrease, while the intensities of the diffraction peaks ($2\theta \approx 25.5^\circ$, 37.9° , 38.6° , 48.1° , 54.0° , 55.1° , 62.7° , 68.8° , 70.4° and 75.1°) of anatase TiO_2 (JCPDS: 01-084-1286) enhance. When the oxidation temperature reaches 700°C , obvious and sharp diffraction peaks ascribed to anatase TiO_2 appear. Meanwhile, the observable diffraction peaks of Ti_3C_2 MXene ($2\theta \approx 9.0^\circ$, 18.3° , 27.7° , 35.2° , 41.5° and 60.8°) still maintain, confirming the coexistence of Ti_3C_2 and TiO_2 in the final product. This is different with the case of oxidation in CO_2 under higher temperature where the XRD peaks of MXene disappeared[21].

Figure 5 shows the SEM images of $\text{TiO}_2/\text{Ti}_3\text{C}_2$ oxidized at different temperatures. Compared with the pristine Ti_3C_2 MXene (Fig. 3b), the surface of $\text{TiO}_2/\text{Ti}_3\text{C}_2$ -300 is basically smooth, and a small number of oxidized particles can be observed at the edge of the sheet, indicating its lower oxidation degree. With the increase of oxidation temperature, the surface of the sample becomes rougher and more nanoparticles can be observed. Correspondingly, the samples show visual expansion in sheet structure and increase interlayer spacing. This is attributed to the increasing formation and growth of TiO_2 nanoparticles as the oxidation temperature increases. However, when the temperature reaches 700°C , the layer structure occurs remarkably swollen, and larger nanoparticles embed into the sheets. It implies the oxidation degree is deep, consistent with the XRD results in Fig. 4. This is due to that the concentration of carbon dioxide diffused into the compact sheets is relatively low at the beginning, so the degree of oxidation of the edge and the surface is higher than that of interlayers. As the oxidation process progresses, the interlayer spacing increases, and carbon dioxide is more likely to spread into the deep sites of the interlayer, causing the oxide particles to gradually grow. The layer spacing is further enlarged and consequently the degree of oxidation is further deepened.

Figure 6 presents TEM images of Ti_3C_2 MXene and $\text{TiO}_2/\text{Ti}_3\text{C}_2$ oxidized at 400°C and 700°C , respectively. It can be clearly seen from Fig. 6a that Ti_3C_2 MXene exhibits a typical accordion layered structure, which is consistent with the morphology observed in the SEM image of Fig. 2b. From the HRTEM image of Ti_3C_2 MXene (Fig. 6b), the interlayer spacing of Ti_3C_2 MXene is about 0.971 nm, which is larger than that of Ti_3AlC_2 , indicating that the Al element in the Ti_3AlC_2 phase has been removed. Furthermore, there are obvious nanoparticles at the edge of the $\text{TiO}_2/\text{Ti}_3\text{C}_2$ -400 sheets (Fig. 6c). The lattice spacing of these nanoparticles measured from the HRTEM image of $\text{TiO}_2/\text{Ti}_3\text{C}_2$ -400 (Fig. 6d) is 0.35 nm, which is ascribed to the (101) crystal plane of anatase TiO_2 . After the oxidation of Ti_3C_2 MXene at 700°C (shown in Fig. 6e), the sheet structure become thinner, and numerous nanoparticles emerge between the sheets. The measured lattice fringe from HRTEM image of $\text{TiO}_2/\text{Ti}_3\text{C}_2$ -700 (Fig. 6f) is also 0.35 nm which corresponds to the (101) crystal plane of anatase TiO_2 . In addition, amorphous carbon emerges at the edge of the nanoparticles after oxidation at 700°C , indicating that Ti_3C_2 MXene transforms to TiO_2 nanoparticles and amorphous carbon, which can be further confirmed by Raman spectra.

In the HRTEM images of $\text{TiO}_2/\text{Ti}_3\text{C}_2$ -700, we detected that Ti_3C_2 MXene formed amorphous carbon after oxidation, but because of the low content and low crystallinity of amorphous carbon, it is difficult to identify it through XRD. Raman spectroscopy was used to determine the TiO_2 and amorphous carbon formation after Ti_3C_2 MXene oxidation at 700°C . Figure 7 shows the Raman spectra of Ti_3C_2 MXene oxidized at 400°C and 700°C . The peaks at 144 cm^{-1} , 198 cm^{-1} , 397 cm^{-1} , 513 cm^{-1} and 638 cm^{-1} are ascribed to the anatase TiO_2 , indicating that Ti_3C_2 MXene has transformed to anatase TiO_2 during oxidation. $\text{TiO}_2/\text{Ti}_3\text{C}_2$ -700 also presents additional two peaks at 1350 cm^{-1} and 1590 cm^{-1} , corresponding to the D and G peaks of carbon, respectively. The D peak is derived from

the defects of the C atomic lattice and the G peak is due to the sp^2 hybrid in-plane stretching vibration of carbon atoms[23, 24]. And the high intensity of D band and the wide bands of D and G indicate the amorphous characteristics of carbon in TiO_2/Ti_3C_2 -700. By contrast, weak peaks of anatase TiO_2 appear, suggesting its lower crystallinity. Meanwhile, the D and G band are also hard to be observed.

In order to compare the variation of chemical bonds in Ti_3C_2 MXene during oxidation process, X-ray photoelectron spectroscopy (XPS) was performed. Figure 8 exhibits the XPS spectra of Ti_3C_2 MXene, TiO_2/Ti_3C_2 -400 and TiO_2/Ti_3C_2 -700, respectively. As shown in Fig. 8a, the surface of Ti_3C_2 MXene obtained by etching with hydrofluoric acid was loaded with abundant oxygen-containing groups and absorbed water. After oxidizing by CO_2 gas, the peak intensity of O-H bond significantly weakened while the peak intensity of the Ti-O bond enhanced (presented in Fig. 8d and g). This is due to the transformation of Ti_3C_2 MXene to TiO_2 and the reduction of the terminal surface functional groups during oxidation process. By comparing the Ti 2p spectra, it is observable Ti $2p_{3/2}$ (454.5 eV) and Ti $2p_{1/2}$ (460.3 eV) peaks assigned to Ti-C bond of Ti_3C_2 gradually transformed to Ti $2p_{3/2}$ (458.9 eV) and Ti $2p_{1/2}$ (465.0 eV) peaks ascribed to Ti-O band of TiO_2 with the increasing of oxidation temperature[25, 26]. Meanwhile, as shown in Figures c, f and i, the C-Ti (281.9eV) bond of Ti_3C_2 MXene gradually faded away after oxidation. It should be noted that both Ti-O and Ti-C bonds can be clearly found in TiO_2/Ti_3C_2 -400, confirming coexist of TiO_2 and Ti_3C_2 MXene. Most interesting, it exhibits abnormal Ti 2p spectra, where the Ti-O bond presented a broaden peak and higher binding energy than pure Ti-O bond. Correspondingly, the peaks ascribed to Ti-C bonds appear at lower binding energy. Therefore, it may be presumed the formation of O-Ti-C bonds, due to that oxygen is more electronegative than carbon, which results in the inhomogeneous distribution of electron cloud in O-Ti-C bond. The higher electronegativity of oxygen causes higher electron density of O-Ti than Ti-C bond, correspondingly slightly increasing the bonding energy of O-Ti bond and decreasing that of Ti-C bond. In term of XPS results, it is confirmed that part of Ti_3C_2 MXene successfully converts to TiO_2 and carbon doping states simultaneously occur in TiO_2/Ti_3C_2 composites.

Table 1
Specific surface areas of Ti_3C_2 MXene and TiO_2/Ti_3C_2 oxidized at different temperatures

Sample	Ti_3C_2 MXene	TiO_2/Ti_3C_2 -300	TiO_2/Ti_3C_2 -400	TiO_2/Ti_3C_2 -500	TiO_2/Ti_3C_2 -600	TiO_2/Ti_3C_2 -700
S_{BET} m^2/g	4.9	5.5	6.8	9.6	22.7	43.1

Table 1 shows the specific surface areas of Ti_3C_2 MXene and its oxidation products at different temperatures. Compared with Ti_3C_2 MXene, the specific surface area of TiO_2/Ti_3C_2 obtained at lower temperature only has a slightly increase, which is mainly due to the formation of TiO_2 nanoparticles. As the oxidation temperature increases, the specific surface areas of the oxidation products are also gradually enhanced. When the oxidation temperature rises to 700°C, the specific surface area reaches $43.1 m^2 g^{-1}$. This is attributed to the expansion of Ti_3C_2 MXene sheets and growth of a large amount of TiO_2 nanoparticles.

Optical absorption properties of Ti_3C_2 MXene and TiO_2/Ti_3C_2 composites

Generally, pure TiO_2 is unable to absorb visible light due to its large band gap, which is also the biggest obstacle in photocatalysis. Inversely, it can be seen from Fig. 9 that $\text{TiO}_2/\text{Ti}_3\text{C}_2$ composites show strong absorption in the visible light region, which is due to the excellent absorption performance of Ti_3C_2 MXene. However, the absorption value of $\text{TiO}_2/\text{Ti}_3\text{C}_2$ -700 in the visible light region remarkably declines. This is ascribed that most of Ti_3C_2 transforms to TiO_2 and the aggregation of TiO_2 nanoparticles on the surface of Ti_3C_2 MXene will inhibit the absorption of Ti_3C_2 MXene for visible light.

The fluorescence spectra are mainly generated by the recombination of photo-generated electrons and holes in the semiconductor, and the recombination efficiency of the electron-hole pair has a great influence on the photocatalytic performance. Therefore, fluorescence spectra are carried out to analyze the efficiency of charge carrier capture, transport and separation of samples. Figure 10 is the fluorescence spectra of Ti_3C_2 MXene, $\text{TiO}_2/\text{Ti}_3\text{C}_2$ oxidized at different temperatures and commercial TiO_2 (P25). It can be clearly seen that the intensity of P25 emission peak is much stronger than that of Ti_3C_2 MXene and $\text{TiO}_2/\text{Ti}_3\text{C}_2$ composites. The emission peak positions of $\text{TiO}_2/\text{Ti}_3\text{C}_2$ oxidized at different temperatures are nearly invariable, but the intensity gradually enhances with the increase of oxidation temperature. This indicates that the electron-hole pair recombination efficiency of $\text{TiO}_2/\text{Ti}_3\text{C}_2$ is much lower than that of pure TiO_2 , and the electron-hole pair combination efficiency of $\text{TiO}_2/\text{Ti}_3\text{C}_2$ increases with the increase of oxidation temperature. This is because the high-conductivity of Ti_3C_2 MXene material contributes to effectively separate photo-generated electrons and holes of TiO_2 . However, with the increase of oxidation temperature, the content of Ti_3C_2 MXene in $\text{TiO}_2/\text{Ti}_3\text{C}_2$ composites gradually decreases, leading to the conductivity decline of the composite and the corresponding increase in recombination efficiency of electrons and holes.

Photocatalytic activity and mechanism of $\text{TiO}_2/\text{Ti}_3\text{C}_2$ composites

The photocatalytic activities of Ti_3C_2 MXene and $\text{TiO}_2/\text{Ti}_3\text{C}_2$ were evaluated by degradation for Rhodamine B solution (30 mg L^{-1}) under visible light irradiation. It can be seen from Fig. 11 that Rhodamine B is almost not degraded on original Ti_3C_2 MXene, P25 and no catalyst. After oxidation in CO_2 , the degradation rates of $\text{TiO}_2/\text{Ti}_3\text{C}_2$ are greatly improve and are greatly higher than that of P25. When the oxidation temperature is 400°C , the photodegradation rate of the $\text{TiO}_2/\text{Ti}_3\text{C}_2$ composite reaches the maximum ($\sim 94\%$). However, as the oxidation temperature further increases, the photodegradation rate conversely decrease.

The proposal mechanism of $\text{TiO}_2/\text{Ti}_3\text{C}_2$ composite is illustrated in Fig. 12. In $\text{TiO}_2/\text{Ti}_3\text{C}_2$ system, TiO_2 nanoparticles as the main photocatalyst can produce photo-generated electrons and holes under visible light irradiation. On the other hand, Ti_3C_2 MXene as the co-catalyst can improve electron transfer ability, promote the electron-hole separation owing to its excellent conductivity. When the oxidation temperature is too low, the amount of TiO_2 generated is less, resulting in insufficient photo-generating electrons and holes. On the contrary, when the temperature is exceedingly high, the content of Ti_3C_2 MXene in the composites greatly decays, resulting in weakening electron transport efficiency and decrease of photocatalytic activity. As a result, the synergetic effects of Ti_3C_2 MXene and TiO_2 will be critical to improve the photocatalytic activity. Consequently, the key approach is to adjust the proper contents of Ti_3C_2 MXene and TiO_2 in $\text{Ti}_3\text{C}_2/\text{TiO}_2$ composites by controlling the oxidation temperature. Moreover, the incorporation of carbon-doping states may also facilitate to enhance the absorption of TiO_2 for visible light and improve the photocatalytic activity.

Conclusions

In summary, carbon doped TiO₂/Ti₃C₂ composite photocatalysts were prepared via one-step oxidation of Ti₃C₂ MXene at relatively low temperature in CO₂ atmosphere. Rhodamine B solution was used as the target pollutants to evaluate the photocatalytic activity of TiO₂/Ti₃C₂ composites under visible light. TiO₂/Ti₃C₂ composites exhibit greatly enhanced photocatalytic performance than original Ti₃C₂ MXene and commercial P25. In addition, the oxidation temperature plays key roles for the composition, structure and photocatalytic activity. Increasing the oxidation temperature will promote the transformation of Ti₃C₂ MXene to TiO₂ and facilitate to enhance the photo-generated electrons and holes. Inversely, the exceedingly high temperature will result in the declining of Ti₃C₂ MXene and deteriorate the separation of electrons and holes. Therefore, the proper content of Ti₃C₂ MXene and TiO₂ will achieve efficient synergistic effects to improve the photocatalytic activity of the composites. Especially, TiO₂/Ti₃C₂ composite oxidized at 400°C provides the highest degradation rate (~ 94%) for Rhodamine B, which has a significant improvement over Ti₃C₂ MXene and P25.

Declarations

Ethics approval and consent to participate The research described in this paper did not involve human participants and/or animals.

Consent for publication: Not applicable.

Availability of data and materials: All data generated or analyzed during this study are included in this published article.

Competing interests: The authors (Kai Chen, Kang Yan, Qun Xie, Hui Zhu, Xuanke Li, Zhijun Dong, Guanming Yuan, Jiang Zhang and Ye Cong) declare that they have no conflict of interest.

Funding: This work was supported by the National Natural Science Foundation of China (grant number 52002296) and supported by China University of Petroleum Beijing State Key Laboratory of Heavy Oil Processing.

Authors' contributions: All authors contributed to the study conception and design. Material preparation, data collection and analysis were performed by Kang Yan and Kai Chen. The first draft of the manuscript was written by Kai Chen and Kang Yan, and all authors commented on previous versions of the manuscript. All authors read and approved the final manuscript.

Acknowledgements: We appreciate the financial supports of the National Natural Science Foundation of China (grant number 52002296) and China University of Petroleum Beijing State Key Laboratory of Heavy Oil Processing.

Authors' information: All authors' affiliation is Hubei Province Key Laboratory of Coal Conversion and New Carbon Materials, Wuhan University of Science and Technology. Chen Kai and Kang Yan are contributed to equal this work. Corresponding authors and E-mail address: Ye Cong (congye@wust.edu.cn) and Hui Zhu (zhuhui@wust.edu.cn).

References

1. D. Wang, G. Yu, Y. Liu, Y. Gogotsi, Y. Wei, J. Mater. Chem. A 5, 24720 (2017)
2. T. Xu, J. Wang, Y. Cong, S. Jiang, Q. Zhang, H. Zhu, Y. Li, X. Li, Chinese Chem. Lett. 31, 1022 (2020)

3. Y. Guan, S. Jiang, Y. Cong, J. Wang, Z. Dong, Q. Zhang, G. Yuan, Y. Li, X. Li, *2D Mater.* 7, 025010 (2020)
4. Y. Guan, R. Zhao, Y. Cong, K. Chen, J. Wu, H. Zhu, Z. Dong, Q. Zhang, G. Yuan, Y. Li, J. Zhang, X. Li, *Chem. Eng. J.* 433, 133582 (2022)
5. K. Chen, Y. Guan, Y. Cong, H. Zhu, K. Li, J. Wu, Z. Dong, G. Yuan, A. Zhang, X. Li, *J. Alloy. Compd.* 906, 164302 (2022)
6. Q. Peng, J. Guo, Q. Zhang, J. Xiang, B. Liu, A. Zhou, R. Liu, Y. Tian, *J. Am. Chem. Soc.* 136, 4113 (2014)
7. P. Das, Z.-S. Wu, *J. Phys: Energy* 2, 032004 (2020)
8. J. Peng, X. Chen, W. J. Ong, X. Zhao, N. Li., *Chem.* 5, 18 (2019)
9. J. Ran, G. Gao, F. T. Li, T. Y. Ma, A. Du, S. Z. Qiao, *Nat. Commun.* 8, 13907 (2017)
10. Q. Zhong, Y. Li, G. Zhang, *Chem. Eng. J.* 409, 128099 (2021)
11. X. Hu, Y. Wang, Z. Ling, H. Song, Y. Cai, Z. Li, D. Zu, C. Li, *Appl. Surf. Science.* 556, 149817 (2021)
12. J. Li, J. Li, C. Wu, Z. Li, L. Cai, H. Tang, Z. Zhou, G. Wang, J. Wang, L. Zhao, S. Wang, *Carbon* 179, 387 (2021)
13. J. Yang, C. Hu, Y. Jin, H. Chen, W. Zhu, X. Zhou, *Res. Chem. Intermed.* 47, 3453 (2018)
14. M. N. Rafat, C. S. Lim, K. Y. Cho, C. H. Jung, W.-C. Oh, *Res. Chem. Intermed.* 47, 3411 (2021)
15. A. Nawaz, P. Saravanan, *Res. Chem. Intermed.* 47, 2339 (2021)
16. X. Y. Zhang, H. P. Li, X. L. Cui, Y. Lin, *J. Mater. Chem.* 20, 2801 (2010)
17. M. Naguib, O. Mashtalir, M. R. Lukatskaya, B. Dyatkin, C. Zhang, V. Presser, Y. Gogotsi, M. W. Barsoum, *Chem. Commun.* 50, 7420 (2014)
18. Y. Gao, L. Wang, A. Zhou, X. Cao, *Mater. Lett.* 150, 62 (2015)
19. K. Yan, Y. Guan, Y. Cong, T. Xu, H. Zhu, X. Li, *Chinese J. Inorg. Chem.* 35, 1203 (2019)
20. B. Ahmed, D. H. Anjum, M. N. Hedhili, Y. Gogotsi, H. N. Alshareef, *Nanoscale* 8, 7580 (2016)
21. W. Yuan, L. Cheng, Y. Zhang, H. Wu, S. Lv, L. Chai, X. Guo, L. Zheng,, *Adv. Mater. Interfaces* 4, 1700577 (2017)
22. M. Alhabeb, K. Maleski, B. Anasori, P. Lelyukh, Y. Gogotsi, *Chem. Mater.* 29, 7633 (2017)
23. F. Wang, X. Ma, P. Zou, G. Wang, Y. Xiong, Y. Liu, F. Ren, X. Xiong, *Surf. Coat. Technol.* 422, 127568 (2021)
24. S. A. M. Chachuli, M. N. Hamidon, M. Ertugrul, M. S. Mamat, O. Coban, F. N. Tuzluca, Y. O. Yesilbag, N. H. Shamsudin, *J. Alloy. Compd.* 882, 160671 (2021)
25. P. Zhang, R. A. Soomro, Z. Guan, N. Sun, B. Xu, *Energy Stor. Mater.* 29, 163 (2020)
26. Y. Wang, Y. Cui, D. Kong, X. Wang, B. Li, T. Cai, X. Li, J. Xu, Y. Li, Y. Yan, H. Hu, M. Wu, Q. Xue, Z. Yan, L. Zhao, W. Xing, *Carbon* 180, 118 (2021)

Figures

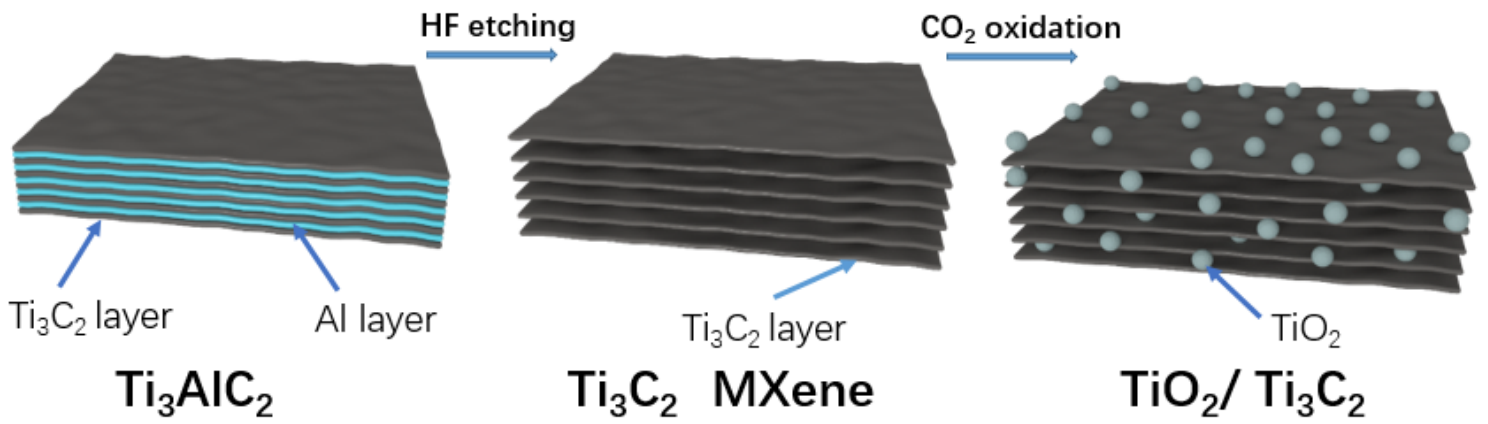


Figure 1

Scheme diagram of preparation of $\text{TiO}_2/\text{Ti}_3\text{C}_2$ composites

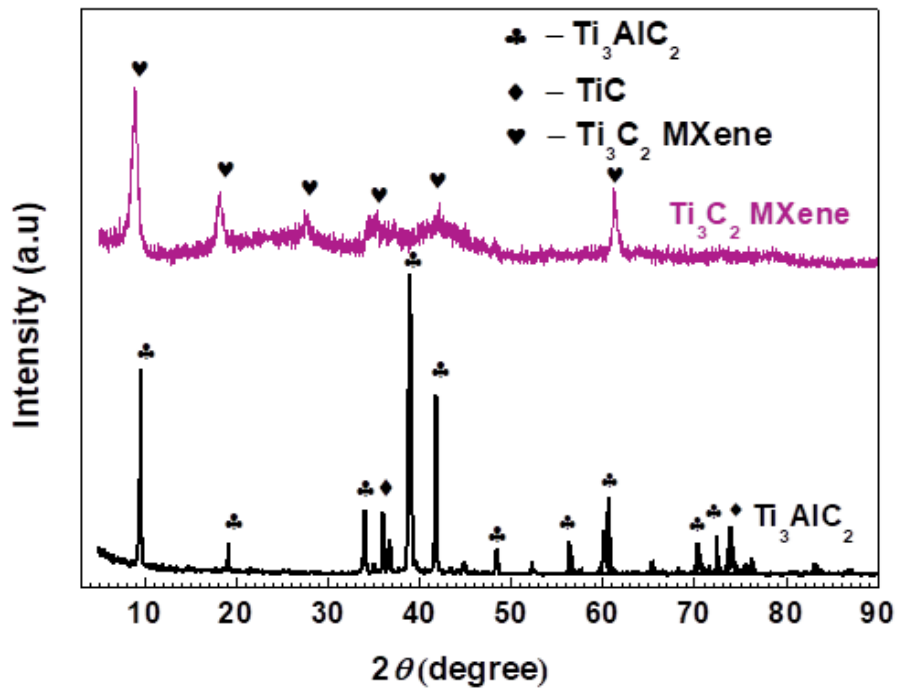


Figure 2

XRD patterns of Ti_3AlC_2 and Ti_3C_2 MXene

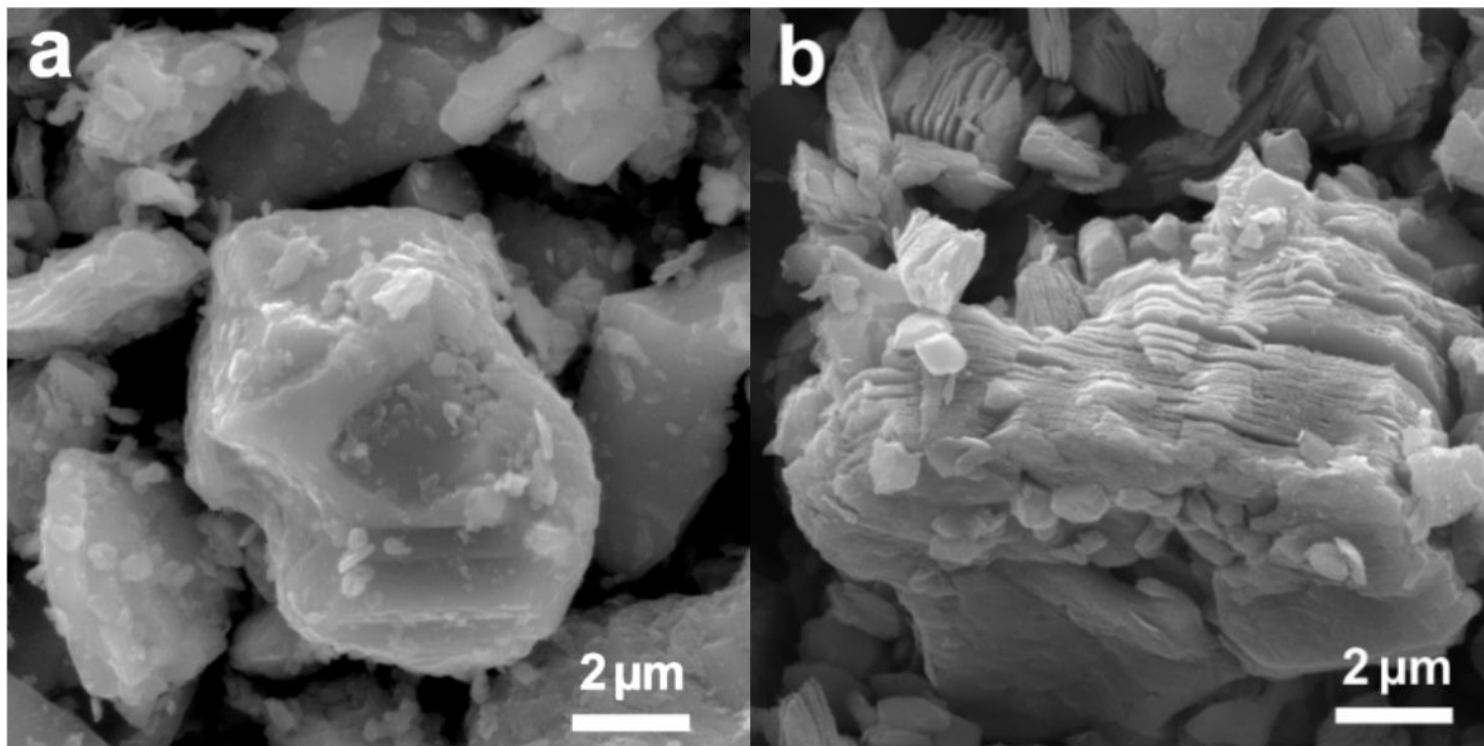


Figure 3

SEM image of (a) Ti_3AlC_2 and (b) Ti_3C_2 MXene

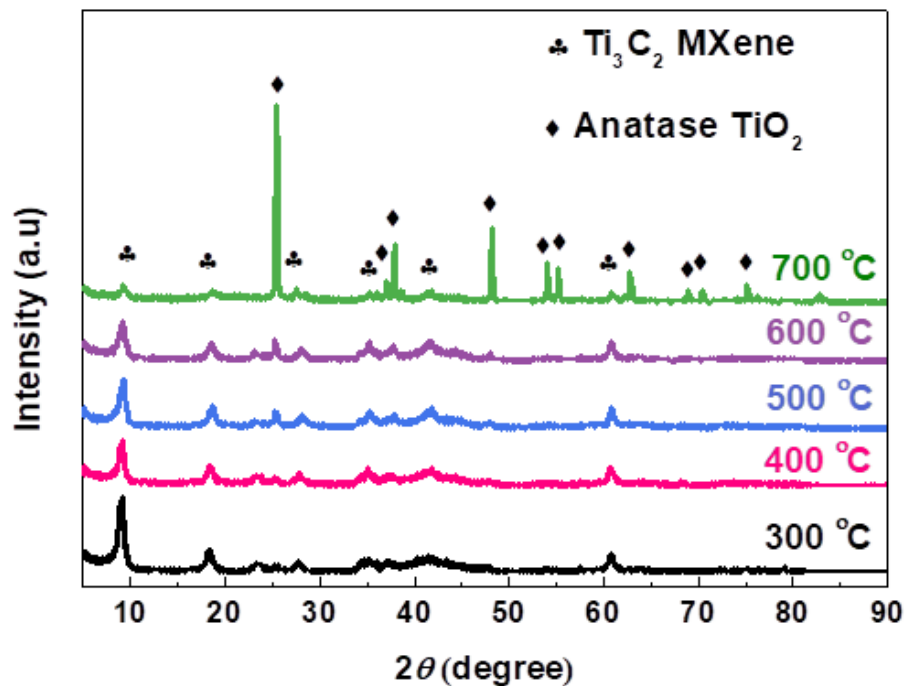


Figure 4

XRD patterns of $\text{TiO}_2/\text{Ti}_3\text{C}_2$ oxidized at different temperatures

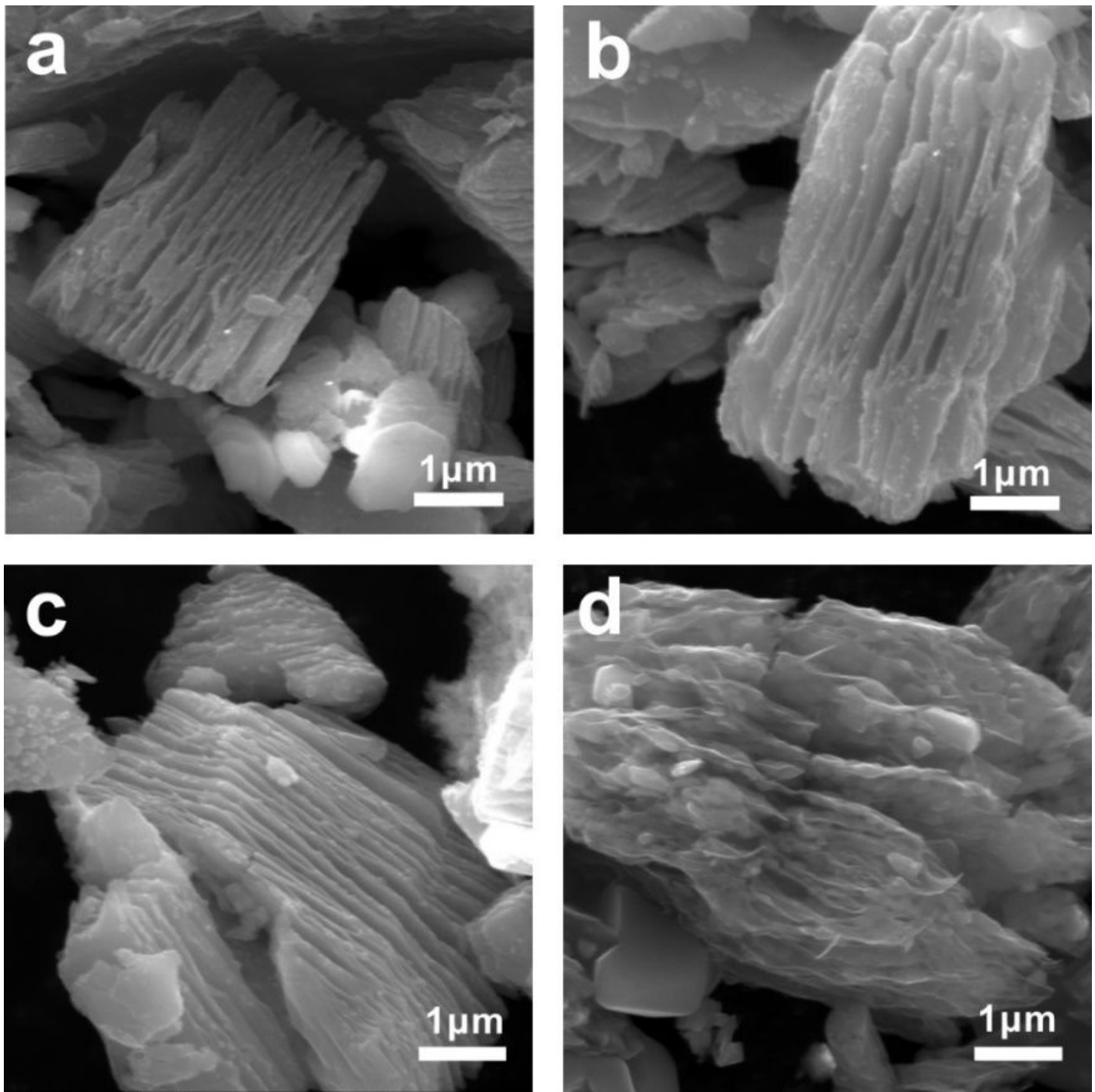


Figure 5

SEM image of TiO₂/Ti₃C₂ oxidized at different temperatures (a) 300 °C, (b) 400 °C, (c) 500 °C, (d) 700 °C

Figure 6

TEM images of (a, b) Ti₃C₂ MXene, (c, d) TiO₂/Ti₃C₂-400 and (e, f) TiO₂/Ti₃C₂-700

Figure 7

Raman spectra of $\text{TiO}_2/\text{Ti}_3\text{C}_2$ -400 and $\text{TiO}_2/\text{Ti}_3\text{C}_2$ -700

Figure 8

The XPS spectra of (a,b,c) Ti_3C_2 MXene, (d,e,f) $\text{TiO}_2/\text{Ti}_3\text{C}_2$ -400 and (g,h,i) $\text{TiO}_2/\text{Ti}_3\text{C}_2$ -700

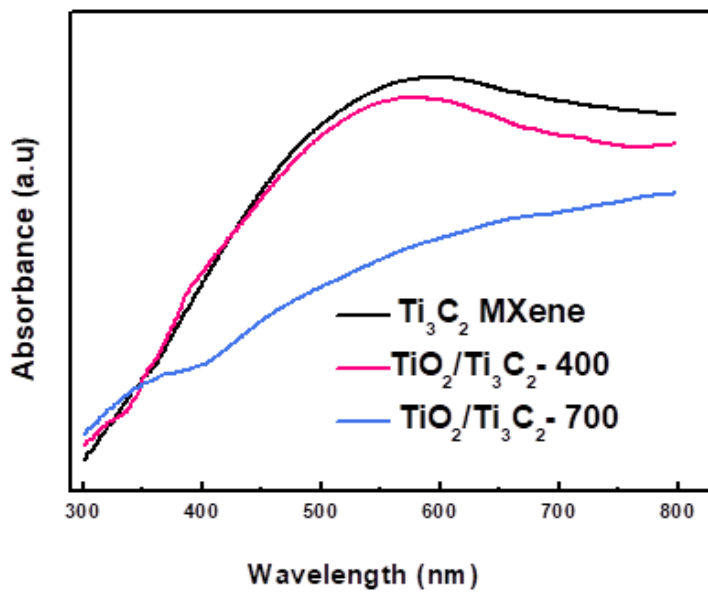


Figure 9

UV-vis diffuse reflection spectra and of Ti_3C_2 MXene, $\text{TiO}_2/\text{Ti}_3\text{C}_2$ -400 and $\text{TiO}_2/\text{Ti}_3\text{C}_2$ -700

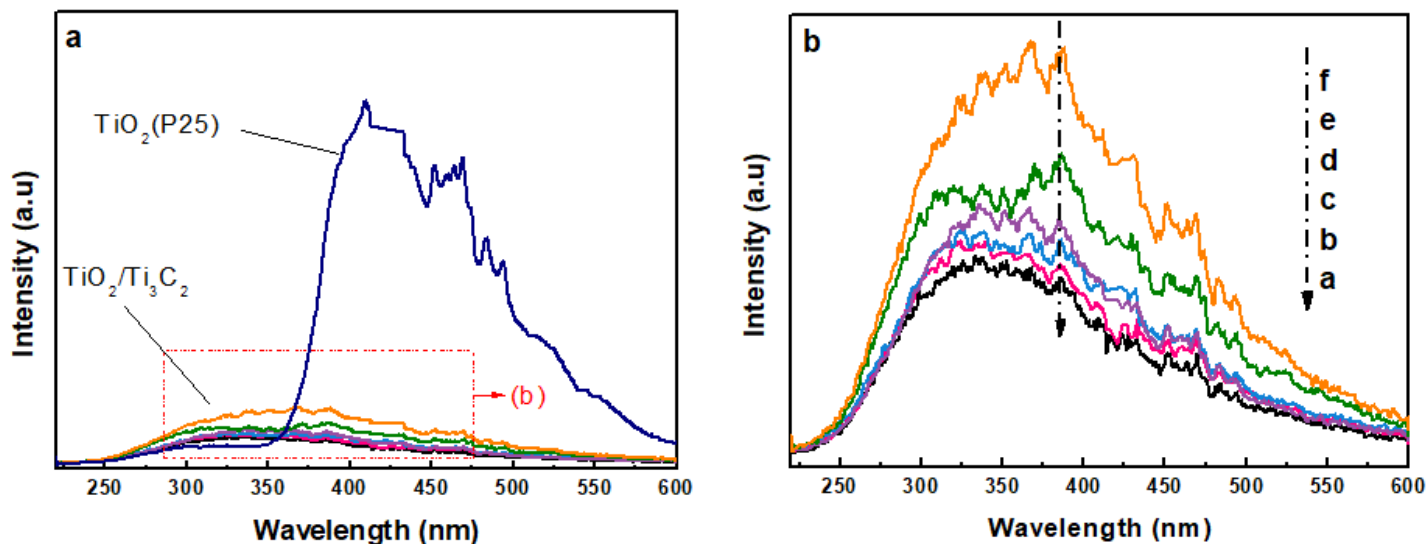


Figure 10

Fluorescence spectra of Ti₃C₂ MXene and TiO₂/Ti₃C₂ oxidized at different temperatures, (a) Ti₃C₂ MXene, (b) 300 °C, (c) 400 °C, (d) 500 °C, (e) 600 °C, (f) 700 °C

Figure 11

Photodegradation rate for Rhodamine B on (a) Ti₃C₂ MXene, (b) TiO₂/Ti₃C₂-300, (c) TiO₂/Ti₃C₂-400, (d) TiO₂/Ti₃C₂-500, (e) TiO₂/Ti₃C₂-600, (f) TiO₂/Ti₃C₂-700, (g) P25, and (h) no catalyst

Figure 12

Mechanism diagram of photocatalytic degradation for Rhodamine B solution on TiO₂/Ti₃C₂ composite